



## Chapter 3.33

**Keywords:** magnetism; sum rules; spin and orbital moments.

# X-ray magnetic circular dichroism

Gerrit van der Laan\*

Diamond Light Source, Harwell Science and Innovation Campus, Didcot OX11 0DE, United Kingdom. \*Correspondence e-mail: gerrit.vanderlaan@diamond.ac.uk

The technique of X-ray magnetic circular dichroism (XMCD) is presented from an experimental perspective. Absorption measurements in a net magnetic field can be performed using circularly polarized X-rays produced by bending magnets or insertion devices at the synchrotron and by employing detection methods such as X-ray transmission, total electron yield or fluorescence yield. XMCD is manifest in absorption edges of open-shell atoms, such as the  $K$ ,  $L_{2,3}$  and  $M_{2,3}$  edges of transition metals, the  $L_{2,3}$ ,  $M_{4,5}$  and  $N_{4,5}$  edges of rare earths and the  $M_{4,5}$ ,  $N_{4,5}$  and  $O_{4,5}$  edges of actinides. The profoundly different characteristic line shapes provide a fingerprint for the spin and orbital character of the valence shell. The integrated intensities over the dichroic absorption edges can be related via sum rules to the expectation values of the spin and orbital magnetic moment in the ground state. The application of these sum rules has transformed XMCD into a powerful technique. This element-, site- and symmetry-specific technique enables a broad range of novel and exciting studies on the electronic and magnetic structure of modern materials.

### 1. Introduction

The effect of magnetic X-ray dichroism was first observed for the Tb  $M_{4,5}$  edge of  $\text{Tb}_3\text{Fe}_5\text{O}_{12}$  at the Laboratoire pour l'Utilisation du Rayonnement Electromagnetique (LURE) at Université Paris-Sud in France (van der Laan *et al.*, 1986) only one year after its prediction (Thole, van der Laan & Sawatzky, 1985). Sum rules relate the integrated intensities of the X-ray magnetic circular-dichroism (XMCD) spectrum to the ground-state expectation values of the orbital and spin magnetic moments (Thole *et al.*, 1992; Carra, Thole *et al.*, 1993). These rules offer a theory-independent analysis which has transformed XMCD into a powerful standard technique, providing invaluable insight into the element-specific microscopic origin of anisotropic magnetic properties, such as the magnetocrystalline effect, the easy direction of magnetization, magnetostriiction, coercivity and magnetic hysteresis.

Dichroism is defined as the polarization dependence of the light absorption by a material. Circular dichroism arises when either space-inversion or time-reversal symmetry is broken in the material. Noncentrosymmetric symmetry allows natural circular dichroism (NCD). In this chapter, we only treat X-ray magnetic circular dichroism (XMCD, also known as CMXD in the older literature) originating from time-reversal symmetry breaking by a net magnetic field.

The XMCD is given as the difference between the two X-ray absorption (XA) signals with the light helicity vector parallel and antiparallel to the net magnetic field. XMCD resembles magneto-optical phenomena in the visible region, such as the Faraday effect. However, since XMCD arises from the excitation of a core electron into an unoccupied valence state, the technique is element-specific. The XMCD originates from electric dipole (or quadrupole) transitions, in which the

#### Related chapters

Volume I: 2.1, 2.8, 2.17, 2.18, 3.10, 4.2, 8.4



OPEN ACCESS

Published under a CC BY 4.0 licence

spin is conserved. It is not caused by magnetic dipole transitions, which are notoriously weak. The sensitivity to the magnetic moment comes from the combined action of the Pauli principle for the valence band and the spin–orbit interaction, which is usually large for the core level.

Because of the optical selection rules, the dipole transitions from the ground state can only reach a limited subset of final states, which means that XA provides a fingerprint of the specific ground state. This makes it a local probe with a high sensitivity to the crystal field, spin–orbit interaction, site symmetry and spin configuration of the valence states (van der Laan & Thole, 1991). The element specificity of XMCD can be used to distinguish between the magnetic contributions from different layers in multilayers or capped particles composed of different elements. It also permits the generation of spatially and magnetically resolved elemental maps (van der Laan & Figueroa, 2014). XMCD offers a means to separate different sites of the same element, especially in ferrimagnets such as ferrites and garnets, where the distinction between different iron sites is facilitated by their antiferromagnetic alignment (Patrick *et al.*, 2002).

The various absorption edges of interest can show rather different characteristics. It is useful to distinguish between the soft and hard X-ray regions, which are separated at around 2–3 keV.

## 2. Instrumental

### 2.1. Production of circularly polarized X-rays

Soft X-ray measurements need to be performed in vacuum to avoid X-ray attenuation by air. For hard X-rays a thin beryllium window can be used to isolate the beamline vacuum from the sample in air or in helium gas, which is less absorbing than air. The more penetrating hard X-rays can be used in extreme environments such as high-pressure cells.

The early way to obtain circularly polarized X-rays was by taking radiation at an ‘inclined angle view’ from the synchrotron. An off-plane view of the electron beam in the bending magnet shows a charge accelerated in an elliptical orbit, whereas an in-plane view shows only a horizontal component. While the emitted radiation is highly polarized, ranging from purely linear in the plane of the orbit to left or right circular below or above the orbit plane, the flux quickly falls off moving away from the orbit plane. For the measurement the figure of merit is  $IP^2$ , with intensity  $I$  and polarization  $P$ .

Third-generation light sources are built around insertion devices (wigglers and undulators), producing a very high intensity beam of X-rays. These devices consist of periodic arrays of magnets, causing the electrons to oscillate around an otherwise straight trajectory. In a helical or elliptical polarization undulator (EPU) the magnetic field vector rotates as electrons pass through the device, resulting in a spiral trajectory about the central axis, and near-100% circular polarization can be obtained in the soft X-ray region at the first undulator harmonic. Although not commonly implemented, fast-polarization switching with frequencies of around 1 Hz is

performed using a fast-kicker system installed between two EPU's to alternate the beam trajectory, where the sample only receives the beam from one undulator at a time.

Hard X-rays are monochromated by Bragg diffraction from high-quality single crystals, preserving linear polarization. The linear polarization from a planar undulator can be converted using a quarter-wave phase plate, which is the method for producing elliptically polarized hard X-rays. A lack of crystals with large  $d$ -spacing means that soft X-rays are monochromated using diffraction gratings, which conserve the polarization. Energy-dispersive monochromators, consisting of a bent crystal or a variable line-spacing grating, can be used to obtain the complete XA spectrum momentarily, which is useful for time-dependent studies, such as of chemical reactions. A micro-focused beam ( $\sim 2 \mu\text{m}$ ) can be obtained using a Kirkpatrick–Baez (KB) mirror pair to study the compositional and spatial variation of complex inhomogeneous materials. Nanosize resolution can be achieved using zone plates or imaging techniques such as photoelectron emission microscopy (PEEM) and transmission X-ray microscopy (TXM).

### 2.2. Magnetic measurement chambers

In the early days of the technique, the sample was magnetized using a nearby permanent magnet, such as  $\text{Nd}_2\text{Fe}_{14}\text{B}$ , which was manually rotated or turned around to obtain the magnetic dichroism (van der Laan *et al.*, 1986; Chen *et al.*, 1990). Nowadays, dedicated magnet chambers exist at practically all synchrotron facilities around the globe.

Two kinds of superconducting magnet design can be distinguished. (i) A split-coil magnet, where coils on opposite sides of the sample holder produce a field along the X-ray beam direction. In some cases, the magnet can be rotated with respect to the beam direction to measure at an angle or in transverse geometry (Dürr *et al.*, 1997). (ii) A superconducting vector magnet, typically reaching fields of 7 T along the beam and 2 T perpendicular to the beam.

Usually, samples can be cooled to  $\sim 2$  K in a helium cryostat. Magnet setups can be equipped with an *in situ* sample-preparation chamber for surface science preparation. Superconducting magnets can have a remanent field up to 300 G, which makes them less suitable if low magnetic fields are required. Often the ramping speed is slow, typically  $\sim 1 \text{ T min}^{-1}$ , although special designs can offer a faster sweeping speed, such as  $\sim 5 \text{ T min}^{-1}$  on ID32 at the ESRF.

To reduce artefacts, the XMCD should ideally be measured for all four combinations of magnetic field and light helicity directions. Electromagnets have the advantage that the magnetization direction can be switched quickly at each photon-energy data point, removing the influence of X-ray beam drift. Using a bipolar power supply, water-cooled copper coils and soft-iron pole pieces, with a centre hole to let the beam pass, magnetic fields of up to  $\pm 2$  T can be achieved with switching times below 0.5 s. Fields along any direction can be produced using an eight-pole electromagnet. Eight conical coils are mounted along the threefold axes of a cube, which leaves the fourfold axes free for access by the beam, sample

holder and detectors. For hard X-rays, the light helicity can be switched quickly by a quarter-wave phase plate.

### 3. Detection methods

Although the absorption coefficients for right- and left-circularly polarized X-rays are measured in the same way as for standard XA, the linearity of the detected signals is important to acquire an undistorted difference spectrum. For hard X-rays the common detection modes are either transmission or fluorescence yield (FY), depending on the relative concentrations of the absorbing atoms. Only transmission measurements can give *absolute* absorption cross sections. Unfortunately, transmission is often not practical for the soft X-ray region due to the high absorbance of the sample. However, the decay of the created core holes after X-ray absorption results in an avalanche of electrons, photons and ions emitted from the sample surface, all of which can be used to measure samples of arbitrary thickness in vacuum.

#### 3.1. X-ray absorption cross section

X-ray absorption cross sections for all elements in the periodic system can be found in Henke's data tables (Henke *et al.*, 1982), which are available from the X-ray database via the website of the Center for X-Ray Optics (<https://cxro.lbl.gov/>). Unfortunately, these tables only list the cross section at off-resonant energies, where the dichroism is much smaller or even absent. Absorption edges due to direct transitions are usually very strong, with a cross section proportional to the number of unoccupied valence states (for example the number of *3d* or *4f* holes) and scale with the overlap between the core and valence wavefunctions. For instance, for Fe  $L_{2,3}$  Henke's tables show a single step change in the attenuation length  $\Lambda = \mu^{-1}$  from 593 nm below the edge to 70 nm above the edge, whereas experimentally  $\Lambda = 16.7$  nm at the  $L_3$  peak maximum (Nakajima *et al.*, 1999). For rare-earth  $M_{4,5}$  edges the absorption lengths are given in Thole, van der Laan, Fuggle *et al.* (1985), for example  $\Lambda = 6.2$  nm for the Gd  $M_5$  peak maximum. For the *3d* metal  $M_{2,3}$  and rare-earth  $N_{4,5}$  giant resonances the absorption cross section is even larger.

#### 3.2. Total electron yield detection

The strong secondary electron emission makes total electron yield (TEY) the preferred detection method in the soft X-ray region. TEY can be monitored either by collecting the emitted electrons, using for example a channel plate, or by measuring the drain current flowing from earth to the grounded sample to compensate the electron emission current. The TEY is a function of the photon energy-dependent X-ray absorption  $\mu(\omega)$  as (Thole, van der Laan, Fuggle *et al.*, 1985)

$$I_{\text{TEY}}(\omega) = C \frac{\mu(\omega)L}{\mu(\omega)L + \cos\theta} = C \frac{L}{L + \Lambda(\omega)\cos\theta}, \quad (1)$$

where  $C$  is a constant lump factor,  $\theta$  is the X-ray incidence angle and  $L$  is the *electron escape depth*, which is approxi-

mately constant over the region of the spectrum, with  $L \simeq 3\text{--}5$  nm for *3d* metal  $L_{2,3}$  (Nakajima *et al.*, 1999) and  $\sim 6$  nm for *4f* metal  $M_{4,5}$  edges (Thole, van der Laan, Fuggle *et al.*, 1985).

In the ideal case where the absorption length  $\Lambda(\omega)$  is much larger than the electron escape depth (*i.e.*  $\mu L \ll \cos\theta$ ), we have  $I = C\mu L/\cos\theta$ , so that the yield is linearly proportional to the absorption coefficient. On the other hand, if the absorption depth is much smaller than the electron escape depth (*i.e.*  $\mu L \gg \cos\theta$ ) then  $I = C$ , so that the absorption structure vanishes.

When  $\Lambda(\omega)$  and  $L$  are comparable in length, the saturation effects curb the intensities of the largest absorption peaks compared with the rest of the spectrum. The absorption peaks become diminished and broadened, and can even show an apparent energy shift. Saturation effects are smaller at normal incidence and are smaller for thinner films. While it is easy to calculate the saturated spectrum from the nonsaturated spectrum, it is unfortunately not easy to do this the other way round, especially since the absorption is different for left- and right-circular polarization.

The short electron escape depth in TEY detection leads to a high surface sensitivity. This makes the spectra sensitive to oxidation, which can show up in the XA as extra features, often a few eV above the main peak, which do not contribute to the XMCD when the oxidized atoms are nonmagnetic. Therefore, most samples require a dedicated treatment, such as *in situ* preparation (evaporation, cleaving, ion sputtering), or alternatively the sample should be capped with a layer of a few nanometres in thickness of an inert material, such as aluminium, gold, platinum or MgO, which however can lead to proximity effects in the magnetic layer. TEY detection is ideal for *in situ* deposited monolayer coverages or magnetic adatoms, and is capable of measuring the XMCD from a coverage of 0.005 of a monolayer.

#### 3.3. Fluorescence yield detection

FY probes deeper than TEY due to a longer escape depth, making this detection less surface sensitive. The FY efficiency is low in the soft X-ray region and a large acceptance angle is essential, which can be achieved by placing the detector close to the sample. However, some FY detectors, which convert X-rays into electrons or electron-hole pairs, can be sensitive to strong magnetic fields.

*Saturation effects* occur in thick or concentrated samples when the X-ray attenuation length is less than or of the order of the escape depth. The longer escape depth makes FY more prone to saturation than TEY. *Self-absorption effects* occur when the emitted photons are re-absorbed before they can exit the sample. Therefore, self-absorption actually acts to prevent saturated absorption from being measured, mitigating the saturation effect. Unfortunately, in the literature the terms saturation and self-absorption are often used interchangeably, which obfuscates matters. It is difficult to correct for both effects, which makes the integrated FY signal in the soft X-ray region unreliable for sum-rule analysis.

## 4. Useful absorption edges of magnetic materials

We will group the absorption edges according to their similar behaviour. Actually, XMCD has also been reported for non-magnetic elements, such as copper and gold, due to hybridization with a magnetic atom, but here we restrict ourselves to the edges of practical interest. Although the  $4d$  and  $5d$  metals are a growing field of interest, so far fewer measurements have been reported.

### 4.1. Soft X-ray region

**4.1.1.  $3d$  metal  $L_{2,3}$ , rare-earth  $M_{4,5}$  and actinide  $N_{4,5}$ ,  $M_{4,5}$  edges.** The strong absorption of the  $3d$  metal  $L_{2,3}$  ( $2p \rightarrow 3d$  at 0.4–1 keV), rare-earth  $M_{4,5}$  ( $3d \rightarrow 4f$  at 0.8–1.5 keV) and actinide  $N_{4,5}$  ( $4d \rightarrow 5f$  at  $\sim 750$  eV for uranium) and  $M_{4,5}$  ( $3d \rightarrow 5f$  at  $\sim 3.5$  keV for uranium) edges is due to dipole-allowed transitions directly into the magnetic valence state. The strong dichroism arises from the large spin–orbit splitting of the core level. The instrumental resolution in the soft X-ray region has a similar width as the core-hole lifetime broadening (a few hundred meV), which allows us to resolve the detailed multiplet structure and charge-transfer satellites.

The XMCD is depicted schematically by a two-step model in Fig. 1(a). In the first step, the absorption of a right- or left-circularly polarized photon ( $\mu_+$  or  $\mu_-$ , respectively) excites a spin-polarized electron from the spin–orbit split  $2p$  level (Fano effect). For the  $2p_{3/2}$  level  $\mu_+$  and  $\mu_-$  give 62.5% and 37.5% spin-up electrons, respectively, while for the  $2p_{1/2}$  level  $\mu_+$  and  $\mu_-$  give 25% and 75% spin-up electrons, respectively. In the second step, the spin-polarized electron has to find a place in the unoccupied  $3d$  band, obeying the Pauli exclusion theorem, which gives a dichroism when the  $3d$  states are spin-polarized.

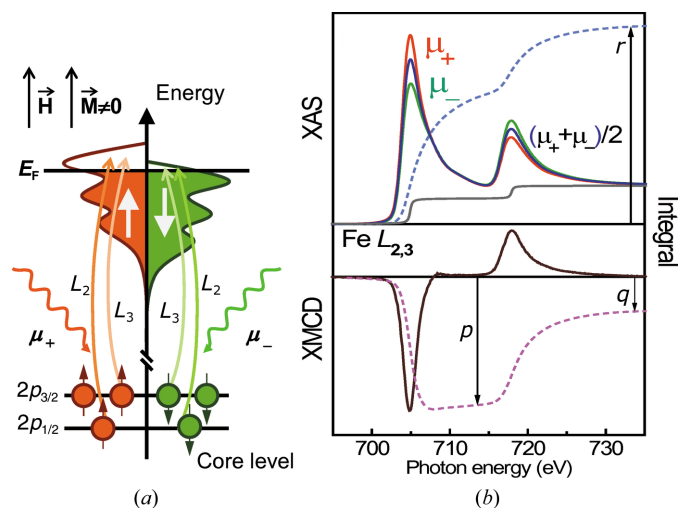


**Figure 1**

XMCD. (a) Schematic picture of the two-step model. Absorption of left ( $\mu_-$ ) and right ( $\mu_+$ ) circularly polarized X-rays exciting an electron from the spin–orbit split  $2p$  core level (Fano effect) into the empty  $3d$  band of a magnetic material (Pauli exclusion principle). (b) Top: XAS at the Fe  $L_{2,3}$  edge for left- and right-circular polarization, together with the difference spectrum: the XMCD. Bottom: the integrated signals  $p$ ,  $q$  and  $r$  over the  $L_{2,3}$  XMCD and XAS which are required for the sum-rule analysis.

In localized many-electron systems, the excitations  $3d^n \rightarrow 2p^5 3d^{n+1}$  for transition metals (or  $4f^n \rightarrow d^9 f^{n+1}$  for  $f$  metals) are self-screening, *i.e.* the additional  $3d$  electron effectively screens the core-hole potential, strongly reducing the charge transfer of valence electrons. The spectra can be adequately modelled using multiplet calculations, where the initial- and final-state configurations are calculated in intermediate coupling, where spin–orbit and electrostatic interactions are on an equal footing. Ligand-field and charge-transfer interactions can be included in these calculations. The input parameters for the spin–orbit interaction and  $2p$ – $3d$  and  $3d$ – $3d$  Coulomb and exchange interactions are obtained from atomic Hartree–Fock (HF) theory (Cowan, 1981). The Slater parameters are typically scaled to 70–80% to account for configuration interaction and electronic screening. Calculated multiplet spectra for XMCD across the full row of elements are available from the literature for  $3d$  metal  $L_{2,3}$  edges (van der Laan & Thole, 1991), rare-earth  $M_{4,5}$  edges (Thole, van der Laan, Fuggle *et al.*, 1985; Goedkoop *et al.*, 1988) and actinide  $M_{4,5}$  and  $N_{4,5}$  edges (Ogasawara *et al.*, 1991; van der Laan & Thole, 1996).

**4.1.2. Giant resonances.** Although the absorption edges of the shallow core levels have been less well studied, recently they have regained interest as they became assessable by the high-harmonic generation of soft X-rays by laser light. The  $3d$  metal  $M_{2,3}$  ( $3p \rightarrow 3d$  at 30–125 eV), rare-earth  $N_{4,5}$  ( $4d \rightarrow 4f$  at 100–175 eV) and actinide  $O_{4,5}$  ( $5d \rightarrow 5f$  at  $\sim 100$  eV for uranium) transitions have much in common. (i) The core spin–orbit interaction is smaller than the core–valence electrostatic interactions. (ii) The core and valence shell have the same principal quantum number, giving a large overlap between their wavefunctions, and hence a large radial matrix element in the transition probability, as well as a short core-hole lifetime (a few eV line-width broadening).

The electric dipole selection rules are  $\Delta J = J' - J = -1, 0, 1$ , where  $J' = J = 0$  is forbidden. In an  $LS$  coupled basis there are additional selection rules:  $\Delta S = S' - S = 0$  and  $\Delta L = L' - L = -1, 0, 1$  with  $L' = L = 0$  forbidden. As an example, Gd  $N_{4,5}$  is shown in Fig. 2(a) (Starke *et al.*, 1997). In the limit of vanishing core spin–orbit coupling, only the three  $^8P_J$  states ( $J = 5/2, 7/2, 9/2$ ) are dipole-allowed from the  $^8S_{7/2}$  ground state of gadolinium. These absorption peaks show an asymmetric Fano line shape due to the interference between the excitation-decay process  $4f^n + \hbar\omega \rightarrow 4d^9 4f^{n+1} \rightarrow 4f^{n-1} \varepsilon$  and the direct photoemission channel  $4f^n + \hbar\omega \rightarrow 4f^{n-1} \varepsilon$ , where  $\varepsilon$  represents a continuum state.

Turning on the small  $4d$  spin–orbit coupling, additional transitions become allowed to states with higher  $L$ , which have a lower energy (Hund's rule). When their energy falls below the continuum onset these transitions appear as sharp peaks in the pre-edge region.

### 4.2. Hard X-ray edges

**4.2.1.  $3d$  metal  $K$  edge.** The  $3d$  metal  $K$  edge (at 5–11 keV) gives complementary information compared with the  $L_{2,3}$  edge, but its dichroism is much smaller, typically  $10^{-3}$  (Schütz

*et al.*, 1987). The  $1s$  core shell lacks spin–orbit interaction, and the dichroism originates from the small spin–orbit splitting in the valence  $p$  state. As the core–valence interaction is small, the spectra usually give a good agreement with the calculated empty  $p$  density of states. Quadrupole transitions to the localized  $3d$  states can cause a pre-edge structure. When the inversion symmetry is broken, the  $3d$  states mix with the  $p$  valence states, which increases the intensity of the pre-peaks.

**4.2.2. Rare-earth  $L_{2,3}$  edges.** In the rare earths the  $L_{2,3}$  edges (5.5–10 keV) are due to dipole transitions from the  $2p$  level to the  $5d$  conduction band, which screens the  $4f$  state. The screening by the  $5d$  electrons plays an important role in the spectral shape of the  $L_{2,3}$  edges, presenting a scenario very different from that of the  $3d$  metal  $L_{2,3}$  edges. The pre-peak is due to quadrupole transitions to the  $4f$  states, which are self-screening.

## 5. Basic formalism

Here, we will establish the relationship between the XMCD signal and the magnetic moment of the sample. The interaction Hamiltonian for an atom with angular quantum numbers  $L$ ,  $S$  and  $J$  in a magnetic field  $\mathbf{B}$  is  $\mathcal{H}_{\text{mag}} = \mu_B(\mathbf{L} + g\mathbf{S}) \cdot \mathbf{B} = \mu_B g_J \mathbf{J} \cdot \mathbf{B}$ , where  $g = 2.0023$  and  $g_J$  is the Landé splitting factor. The Zeeman field lifts the  $(2J + 1)$  degeneracy of the  $J$  level, splitting it into sublevels  $M = -J, -J + 1, \dots, J$ . An electron in a sublevel  $M$  has a magnetic energy  $E_M = \mu_B g_J M B_z$ , where the Bohr magneton,  $\mu_B = e\hbar/(2mc)$ , is a positive number, so that in a field  $B_z$  the lowest ground state has  $M_L = -L$ ,  $M_S = -S$  and  $M = -J$ .

The magnetic moment  $\mathcal{M}_z$  is

$$\mathcal{M}_z = \mu_L + \mu_S = \mu_J = -\frac{\mu_B}{\hbar} g_J \langle J_z \rangle, \quad (2)$$

where the expectation value of the total angular momentum  $\langle J_z \rangle = \sum_M n_M M$  (in units  $\mu_B/\hbar$ , which are usually omitted) is negative for the moments aligned along the field, since the negative  $M$  levels are filled first.  $\mathcal{M}_z$  having the opposite sign to the angular momentum arises from the classical definition of the magnetic moment caused by an orbiting electron with negative charge. Hence,  $\mathcal{M}_z$  has the same sign as  $B_z$ .

The electric dipole transition probability is given by the Wigner–Eckart theorem as (omitting the radial part)

$$\sum_{M'} |\langle J'M' | C_q^{(1)} | JM \rangle|^2 = \sum_{M'} \begin{pmatrix} J' & 1 & J \\ -M' & q & M \end{pmatrix}^2 |\langle J' || C^{(1)} || J \rangle|^2, \quad (3)$$

where the initial electronic state  $|JM\rangle$  is the ket (*in-state*) and the final state  $|J'M'\rangle$  is the bra (*out-state*); therefore, the left component in the  $3j$ -symbol is the conjugate  $M'^* = -M'$ . The  $3j$ -symbol gives the angular momentum selection rules for XMCD:

$$\begin{aligned} \Delta J = J' - J &= -1, 0, +1 \quad \text{with } J' = J = 0 \text{ forbidden,} \\ q = \Delta M = M' - M &= -1, 0, +1. \end{aligned} \quad (4)$$

It is usual to define the XMCD signal,  $\Delta\mu$ , as the difference between antiparallel and parallel orientations of the sample magnetization  $B$  and the incident photon helicity,

$$\Delta\mu \equiv \mu_{\uparrow\downarrow} - \mu_{\uparrow\uparrow} = \mu_-(B) - \mu_+(B) = \mu_+(-B) - \mu_-(-B), \quad (5)$$

where the subscript in  $\mu_{\pm}$  represents the sign of  $q = \pm 1$ . Because of time-reversal symmetry,  $\Delta\mu$  is the same if both the field and helicity are reversed.

The definition of equation (5) means that, for example, for ferromagnetic iron, copper and nickel the  $L_3$  peak is negative

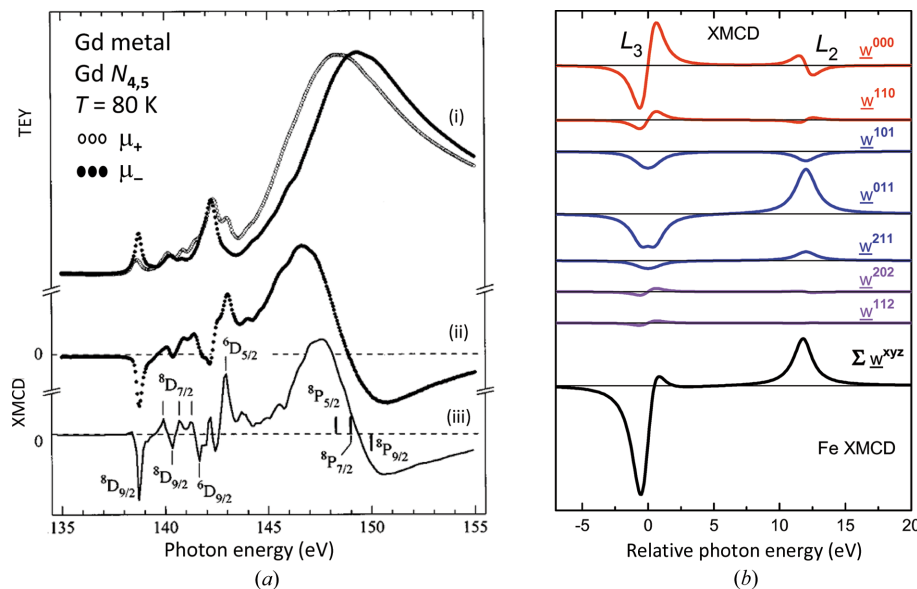


**Figure 2**

(a) Gd  $N_{4,5}$  absorption spectra: (i) spectra measured for parallel and antiparallel orientations of photon helicity and magnetization and (ii) experimental and (iii) calculated XMCD spectra ( $\mu_+ - \mu_-$ ) (Starke *et al.*, 1997). (b) Relative contributions to the Fe  $2p$  XMCD spectrum from the different ground-state moments  $\langle \underline{w}^{xyz} \rangle$  for metallic iron. The blue spectra fulfil the sum rules for orbital and spin magnetic moments. The bottom spectrum gives the sum over all contributions and resembles the experimental Fe  $L_{2,3}$  XMCD spectrum. For further details, see van der Laan (1997).

**Table 1**

Relations between  $LS$ -coupled tensor operators  $w^{xyz}$  and standard ground-state operators,  $S_z = \sum_i s_{z,i}$ ,  $L_z = \sum_i l_{z,i}$ ,  $T_z = \frac{1}{4}(3[l_z(l \cdot s)]_+ - 2l^2 s_z)_i$ ,  $Q_{zz} = \sum_i (l_z^2 - \frac{1}{3}l^2)_i$ ,  $P_{zz} = \sum_i (l_z s_z - \frac{1}{3}l \cdot s)_i$  and  $R_{zz} = \frac{1}{3} \sum_i [5l_z(l \cdot s)l_z - (l^2 - 2)l \cdot s - (2l^2 + 1)l_z s_z]_i$ .

Operator name	$w^{xyz}$	$d$ shell	$f$ shell
Number operator	$w^{000} = n$	$n$	$n$
Spin-orbit coupling	$w^{110} = (ls)^{-1} \sum_i l_i \cdot s_i$	$l \cdot s$	$\frac{2}{3}l \cdot s$
Spin moment	$w_0^{011} = -s^{-1} S_z$	$-2S_z$	$-2S_z$
Orbital moment	$w_0^{101} = -l^{-1} L_z$	$-\frac{1}{2}L_z$	$-\frac{1}{3}L_z$
Magnetic dipole term	$w_0^{211} = -(2l+3)l^{-1} T_z$	$-\frac{7}{2}T_z$	$-3T_z$
Quadrupole moment	$w_0^{202} = 3[l(2l-1)^{-1}]Q_{zz}$	$\frac{1}{2}Q_{zz}$	$\frac{1}{5}Q_{zz}$
	$w_0^{112} = 3l^{-1}P_{zz}$	$\frac{3}{2}P_{zz}$	$P_{zz}$
	$w_0^{312} = 3[(l-1)(2l-1)^{-1}]R_{zz}$	$R_{zz}$	$\frac{3}{10}R_{zz}$

(see Fig. 1). For instance, consider the transition  $\text{Ni } 3d^9 \rightarrow 2p^5 3d^{10}$  for a spherical atom in a field  $B_z$ . At  $T = 0$  K the electronic configuration  $3d^9$  has ground state  ${}^2D_{5/2}$  ( $M = -5/2$ ). The  $2p$  core hole in the final state has  $|M'| \leq 3/2$ . For the transition  $|M = -5/2\rangle \rightarrow |M' = -3/2\rangle$  only  $q = M' - M = +1$  is allowed. Using the definition in equation (5), we indeed obtain  $\Delta\mu = \mu_-(B) - \mu_+(B) < 0$ . At finite temperature, higher  $M$  levels will also be populated, reducing the XMCD signal. However, the opposite sign of the XMCD is only obtained for a population inversion of the magnetic levels in the ground state (Thole, van der Laan & Sawatzky, 1985).

## 6. Sum-rule analysis

We will present the sum rules from the general perspective of angular momentum transfer from the photon to a core electron which is excited to a partially filled valence state in a multi-electronic configuration. By summing over the transitions from all levels of the core hole its properties drop out and the total intensity becomes proportional to the spin and orbital moments of the ground state.

For a magnetic material, the electronic shell  $l$  is characterized by a complete set of  $LS$ -coupled multipole moments  $\langle w^{xyz} \rangle$ , in which the orbital moment  $x$  and the spin moment  $y$  are coupled to a total moment  $z$ . Moments with even  $x$  describe the shape of the charge distribution and those with odd  $x$  describe the orbital motion. The tensors for the  $d$  and  $f$  shells up to  $z = 2$ , expressed as standard tensors, are given in Table 1. We furthermore define coupled moments over the *hole state*, denoted by an underscore, where  $\langle \underline{w}^{xyz} \rangle = -\langle w^{xyz} \rangle$ , except that  $\langle \underline{w}^{000} \rangle + \langle w^{000} \rangle = 4l + 2$ .

We define the fundamental spectra  $I^z$  as linear combinations over the polarized  $I_q$  spectra, where  $I^0 = I_{-1} + I_0 + I_1$ ,  $I^1 = I_{-1} - I_1$  and  $I^2 = I_{-1} - 2I_0 + I_1$  are the isotropic spectrum, XMCD and X-ray magnetic linear dichroism (XMLD), respectively ( $q = 0$  corresponds to linear polarization along the quantization axis). These spectra will depend on the ground-state tensors  $\langle \underline{w}^{xyz} \rangle$ . Fig. 2(b) shows the contributions from each  $\langle \underline{w}^{xyz} \rangle$  to the Fe  $L_{2,3}$  XMCD spectrum of metallic iron, which were calculated by assuming an independent particle model for the  $3d$  states and a core level  $j_c$  split by an effective exchange interaction (van der Laan, 1997). It is seen that for each tensor the integrated intensity of the XMCD vanishes,

except for  $\langle \underline{w}^{101} \rangle$ . The separate integrals over the  $L_3$  and  $L_2$  edges vanish for all tensors except those with  $z = 1$ . Nevertheless, the other tensors still show an asymmetric line shape for each edge. Summing over all  $\langle \underline{w}^{xyz} \rangle$  contributions gives a spectrum that resembles the iron XMCD in Fig. 1.

The above result can be generalized by formulating the sum rules. For an electron excited from a core level with orbital, spin and angular quantum numbers  $c, \frac{1}{2}, j_c$  to a valence shell  $l = c + 1$ , the intensity of the  $j_c^\pm = c \pm \frac{1}{2}$  core levels can be written as (Carra, König *et al.*, 1993; van der Laan, 1999)

$$I_{j_c^\pm}^z = \left\{ \frac{1}{2} [j_c^\pm] \pm \frac{cz}{[z]} \langle \underline{w}^{(z-1)1z} \rangle \pm \frac{c(z+1)}{[z]} \langle \underline{w}^{(z+1)1z} \rangle \right\} |P_{j_c^\pm}|^2, \quad (6)$$

where  $[z]$  is shorthand for  $(2z + 1)$ . Taking the reduced matrix elements  $P_{j_c^\pm}$  to be equal and omitting them in the following, the integrated signals of the sum,  $\rho^z$ , and weighted difference,  $\delta^z$ , over the two edges are related to spin-independent ( $y = 0$ ) and spin-dependent ( $y = 1$ ) ground-state moments, respectively:

$$\rho^z \equiv I_{j_c^+}^z + I_{j_c^-}^z = [c] \langle \underline{w}^{z0z} \rangle, \quad (7)$$

$$\delta^z \equiv I_{j_c^+}^z - \frac{c+1}{c} I_{j_c^-}^z = [c] \frac{z}{[z]} \langle \underline{w}^{(z-1)1z} \rangle + [c] \frac{z+1}{[z]} \langle \underline{w}^{(z+1)1z} \rangle. \quad (8)$$

From this general formulation we obtain the specific sum rules such as, for  $p \rightarrow d$ ,

$$\frac{\delta^0}{\rho^0} = \frac{\langle \underline{w}^{110} \rangle}{\langle \underline{w}^{000} \rangle} \rightarrow \frac{\rho_{L_3}^0 - 2\rho_{L_2}^0}{\rho_{L_3}^0 + \rho_{L_2}^0} = -\frac{\langle l \cdot s \rangle}{n_h}, \quad (9)$$

$$\frac{\rho^1}{\rho^0} = \frac{\langle \underline{w}^{101} \rangle}{\langle \underline{w}^{000} \rangle} \rightarrow \frac{\rho_{L_3}^1 + \rho_{L_2}^1}{\rho_{L_3}^0 + \rho_{L_2}^0} = \frac{1}{2} \frac{\langle L_z \rangle}{n_h}, \quad (10)$$

$$\frac{\delta^1}{\rho^0} = \frac{\langle \underline{w}^{011} \rangle + 2\langle \underline{w}^{211} \rangle}{3\langle \underline{w}^{000} \rangle} \rightarrow \frac{\rho_{L_3}^1 - 2\rho_{L_2}^1}{\rho_{L_3}^0 + \rho_{L_2}^0} = \frac{2}{3} \frac{\langle S_z \rangle}{n_h} + \frac{7}{3} \frac{\langle T_z \rangle}{n_h}, \quad (11)$$

where  $\rho^0 = \rho_1 + \rho_0 + \rho_{-1}$  and  $\rho^1 = \rho_1 - \rho_{-1}$  are the integrated intensities of the isotropic spectrum and XMCD over the  $L_3$  and  $L_2$  edges. The right-hand sides are obtained using the standard operators for the  $d$  shell given in Table 1. It is seen that the ratio  $\rho^1/\delta^1$  is independent of  $n_h$ .

By a simple change in notation (Chen *et al.*, 1995), namely  $m_L = -\langle L_z \rangle$ ,  $m_{S_{\text{eff}}} = -2\langle S_{z,\text{eff}} \rangle = -2\langle S_z \rangle - 7\langle T_z \rangle$ ,  $p = \rho_{L_3}^1$ ,  $q = \rho_{L_3}^1 + \rho_{L_2}^1$  and  $r = \rho_{-1} + \rho_{+1} \simeq \frac{2}{3}\rho^0$ , the sum rules for  $p \rightarrow d$  can also be written as

$$m_L = -\frac{4q}{3r} n_h \quad \text{and} \quad m_{S_{\text{eff}}} = -\frac{6p - 4q}{r} n_h. \quad (12)$$

To apply these sum rules to the experimental data, we take the integrals over the absorption edges after the removal of a background due to transitions into higher unoccupied and continuum states. This procedure is shown in Fig. 1(b), where for both  $L_3$  and  $L_2$  edges a step function, convoluted by a Voigt line shape, is subtracted from the spectrum. The integrals over the XA and XMCD give the values of  $p$ ,  $q$  and  $r$  that are used in equation (12). In the case of less pronounced

absorption peaks a reference spectrum of a similar element with a well known number of holes should be subtracted. For instance, a relative comparison between the XA of gold and platinum allows us to separate the unoccupied platinum  $5d$  states (or the XA of silver to separate the palladium  $4d$  states; van der Laan & Figueroa, 2014).

The spin sum rule requires a separate integration over the  $L_3$  and  $L_2$  edges. Therefore, this rule is only strictly valid if  $j_c$  is a good quantum number, which is fulfilled when the core spin-orbit interaction is much larger than the core–valence interaction. This holds reasonably well for the Fe, Co and Ni  $L_{2,3}$  spectra. However, a correction factor is needed for vanadium, chromium and manganese, which not only depends on the element but also on the  $3d$  (de)localization, crystal field and hybridization (Thole & van der Laan, 1988). The rare-earth  $M_{4,5}$  spectra also require a large correction factor.

Theoretical limitations for the sum rule are the assumption of constant and spin-independent radial matrix elements, the need to estimate the number of holes, the possible mixing of dipole and quadrupole moments and the contribution from both  $l = c \pm 1$  channels. Experimental errors can occur due to saturation effects, the choice of integration limits, using the sum spectra,  $(I_{-1} + I_1)$ , instead of the isotropic spectrum for normalization or using the asymmetry,  $(I_{-1} - I_1)/(I_{-1} + I_1)$ , which depends on the linear dichroism, instead of the XMCD.

## 7. Field-dependent XMCD

XMCD offers the unique possibility of *element-specific magnetic hysteresis* measurements, which allow the separation of the contributions from different chemical species. This consists of measuring the magnetization  $M$  using the XMCD at a fixed photon energy as a function of the applied magnetic field  $H$ . The results can be converted into an Arrott plot, which shows the isothermal variation of  $M^2$  as a function of  $H/M$ . By comparing Arrott plots measured at different temperatures, an accurate estimation of the Curie temperature can be obtained (Baker *et al.*, 2015).

The TEY signal can be sensitive to the applied magnetic field, which can be verified and corrected by repeating the hysteresis measurement at an off-resonance energy. Good results are also obtained with FY detection, if saturation effects are taken for granted.

## 8. Time-dependence

XA, and hence XMCD, acts as the initial step in coherent second-order processes such as resonant photoemission (RESPES) and resonant inelastic X-ray scattering (RIXS). Monitoring the decay processes in the second step gives information about the de-excitation of the intermediate core-hole state reached from the ground state. This can provide an unambiguous assignment of the different configurations in mixed-valence and hybridized compounds. In itinerant systems, such as the  $3d$  transition metals, the femtosecond time scale of the core-hole clock can be used to monitor the electronic screening processes. The XMCD in RIXS shows that

the  $2p$  core hole in metallic iron and cobalt is screened within the  $\sim 1$  fs lifetime, whereas in metallic nickel, which has a narrow  $3d$  band, the core hole is only incompletely screened.

In localized systems the X-ray transition is faster than the time it takes for the valence electrons to rearrange. For example, in the Fe  $L_{2,3}$  XMCD of magnetite ( $\text{Fe}_3\text{O}_4$ ) the  $\text{Fe}^{2+}$  and  $\text{Fe}^{3+}$  cations in the octahedral sites are perceived as ‘frozen’, allowing their relative occupations to be measured (Patrick *et al.*, 2002). This is in contrast to the much slower time scale of Mössbauer spectroscopy, which detects an average valence of +2.5 for the octahedral sites.

On the picosecond time scale of the precessional motion of the spin, the magnetization dynamics can be recorded using X-ray-detected ferromagnetic resonance (XFMR), where the XMCD effect is used as a stroboscopic probe to measure the precessing spins (Marcham *et al.*, 2013). By exploiting the time structure of the pulsed synchrotron radiation from the storage ring, the relative phase of precession in the individual magnetic layers of a multilayer stack or spin valve can be determined (van der Laan *et al.*, 2017).

The advent of X-ray free-electron lasers enables the study of the element-specific magnetization dynamics on a femtosecond time scale using XMCD and XMLD.

## 9. Conclusions

XMCD offers large advantages, such as element specificity, spin and orbital moment analysis, magnetic anisotropy determination, surface sensitivity and time-domain resolution. The XMCD effect has found widespread application in magnetic imaging techniques, such as PEEM using TEY, Fourier transform holography (FTH) using X-ray scattering, or TXM with spatial resolutions of typically tens of nanometres.

XMCD has become one of the most versatile techniques to study the electronic and magnetic structure of diverse materials, ranging from nanoparticles, molecular magnets, organometallic complexes and dilute magnetic semiconductors to doped topological insulators.

Time-resolved XMCD with femtosecond laser excitation can be used to study magnetic switching, giving information on the driving force behind femtosecond spin–lattice relaxation.

## References

- Baker, A. A., Figueroa, A. I., Kummer, K., Collins-McIntyre, L. J., Hesjedal, T. & van der Laan, G. (2015). *Phys. Rev. B*, **92**, 094420.
- Carra, P., König, H., Thole, B. T. & Altarelli, M. (1993). *Physica B*, **192**, 182–190.
- Carra, P., Thole, B. T., Altarelli, M. & Wang, X. (1993). *Phys. Rev. Lett.* **70**, 694–697.
- Chen, C. T., Idzerda, Y. U., Lin, H.-J., Smith, N. V., Meigs, G., Chaban, E., Ho, G. H., Pellegrin, E. & Sette, F. (1995). *Phys. Rev. Lett.* **75**, 152–155.
- Chen, C. T., Sette, F., Ma, Y. & Modesti, S. (1990). *Phys. Rev. B*, **42**, 7262–7265.
- Cowan, R. D. (1981). *The Theory of Atomic Structure and Spectra*. Berkeley: University of California Press.
- Dürr, H. A., Guo, G. Y., van der Laan, G., Lee, J., Lauhoff, G. & Bland, J. A. C. (1997). *Science*, **277**, 213–215.

- Goedkoop, J. B., Thole, B. T., van der Laan, G., Sawatzky, G. A., de Groot, F. M. F. & Fuggle, J. C. (1988). *Phys. Rev. B*, **37**, 2086–2093.
- Henke, B. L., Lee, P., Tanaka, T. J., Shimabukuro, R. L. & Fujikawa, B. K. (1982). *At. Data Nucl. Data Tables*, **27**, 1–144.
- Laan, G. van der (1997). *Phys. Rev. B*, **55**, 8086–8089.
- Laan, G. van der (1999). *Phys. Rev. Lett.* **82**, 640–643.
- Laan, G. van der (2017). *J. Electron Spectrosc. Relat. Phenom.* **220**, 137–146.
- Laan, G. van der & Figueroa, A. I. (2014). *Coord. Chem. Rev.* **277–278**, 95–129.
- Laan, G. van der & Thole, B. T. (1991). *Phys. Rev. B*, **43**, 13401–13411.
- Laan, G. van der & Thole, B. T. (1996). *Phys. Rev. B*, **53**, 14458–14469.
- Laan, G. van der, Thole, B. T., Sawatzky, G. A., Goedkoop, J. B., Fuggle, J. C., Esteva, J. M., Karnatak, R. C., Remeika, J. P. & Dabkowska, H. A. (1986). *Phys. Rev. B*, **34**, 6529–6531.
- Marcham, M. K., Shelford, L. R., Cavill, S. A., Keatley, P. S., Yu, W., Shafer, P., Neudert, A., Childress, J. R., Katine, J. A., Arenholz, E., Telling, N. D., van der Laan, G. & Hicken, R. J. (2013). *Phys. Rev. B*, **87**, 180403.
- Nakajima, R., Stöhr, J. & Idzerda, Y. U. (1999). *Phys. Rev. B*, **59**, 6421–6429.
- Ogasawara, H., Kotani, A. & Thole, B. T. (1991). *Phys. Rev. B*, **44**, 2169–2181.
- Patrick, R. A. D., van der Laan, G., Henderson, C. M. B., Kuiper, P., Dudzik, E. & Vaughan, D. J. (2002). *Eur. J. Mineral.* **14**, 1095–1102.
- Schütz, G., Wagner, W., Wilhelm, W., Kienle, P., Zeller, R., Frahm, R. & Materlik, G. (1987). *Phys. Rev. Lett.* **58**, 737–740.
- Starke, K., Navas, E., Arenholz, E., Hu, Z., Baumgarten, L., van der Laan, G., Chen, C. T. & Kaindl, G. (1997). *Phys. Rev. B*, **55**, 2672–2675.
- Thole, B. T., Carra, P., Sette, F. & van der Laan, G. (1992). *Phys. Rev. Lett.* **68**, 1943–1946.
- Thole, B. T. & van der Laan, G. (1988). *Phys. Rev. B*, **38**, 3158–3171.
- Thole, B. T., van der Laan, G., Fuggle, J. C., Sawatzky, G. A., Karnatak, R. C. & Esteva, J. M. (1985). *Phys. Rev. B*, **32**, 5107–5118.
- Thole, B. T., van der Laan, G. & Sawatzky, G. A. (1985). *Phys. Rev. Lett.* **55**, 2086–2088.